Earth, Moon, and Planets (2005) 96: 119–147
DOI 10.1007/s11038-005-9058-2

THE ATMOSPHERES OF SATURN AND TITAN IN THE NEAR-INFRARED: FIRST RESULTS OF CASSINI/VIMS

K. H. BAINES, T. W. MOMARY, B. J. BURATTI, D. L. MATSON and R. M. NELSON
Jet Propulsion Laboratory, California Institute of Technology, 4800 Oak Grove Drive, Pasadena, CA, 91109, USA
(E-mail: kbaines@aloha.jpl.nasa.gov)

P. DROSSART and B. SICARDY
Observatoire de Paris, Meudon, France

V. FORMISANO, G. BELLUCCI and A. CORADINI
Istituto di Fisica dello Spazio Interplanetario, CNR, Rome, Italy

C. GRIFFITH and R. H. BROWN
Lunar and Planetary Lab and Stewart Observatory, University of Arizona, Tucson, AZ, USA

J. P. BIBRING and Y. LANGEVIN
Institut d'Astrophysique Spatiale, Universite de Paris, Paris, France

F. CAPACCIONI and P. CERRONI
Istituto di Astrofisica Spaziale e Fisica Cosmica, CNR, Rome, Italy

R. N. CLARK
U.S. Geological Survey, Denver, CO, USA

M. COMBES
Department De Recherche Spatial, Centre National de la Recherche Scientifique, Meudon, France

D. P. CRUIKSHANK
NASA Ames Research Center, Moffett Field, CA, USA

R. JAUMANN
Institute for Planetary Exploration, DLR, Koln, Germany

T. B. MCCORD
Department of Earth and Space Sciences, University of Washington, Washington, DC, USA

V. MENNELLA
INAF-Osservatorio Astronomico di Capodimonte, Catania, Italy

P. D. NICHOLSON
Astronomy Department, Cornell University, Ithaca, NY, USA

C. SOTIN
Laboratoire de Planetologie et Geodinamique, Universite de Nantes, Nantes, France

Abstract. The wide spectral coverage and extensive spatial, temporal, and phase-angle mapping capabilities of the Visual Infrared Mapping Spectrometer (VIMS) onboard the Cassini-Huygens Orbiter are producing fundamental new insights into the nature of the atmospheres of Saturn and Titan. For both bodies, VIMS maps over time and solar phase angles provide information for a multitude of atmospheric constituents and aerosol layers, providing new insights into atmospheric structure and dynamical and chemical processes. For Saturn, salient early results include evidence for phosphine depletion in relatively dark and less cloudy belts at temperate and mid-latitudes compared to the relatively bright and cloudier Equatorial Region, consistent with traditional theories of belts being regions of relative downwelling. Additional Saturn results include (1) the mapping of enhanced trace gas absorptions at the south pole, and (2) the first high phase-angle, high-spatial-resolution imagery of CH_4 fluorescence. An additional fundamental new result is the first nighttime near-infrared mapping of Saturn, clearly showing discrete meteorological features relatively deep in the atmosphere beneath the planet's sunlit haze and cloud layers, thus revealing a new dynamical regime at depth where vertical dynamics is relatively more important than zonal dynamics in determining cloud morphology. Zonal wind measurements at deeper levels than previously available are achieved by tracking these features over multiple days, thereby providing measurements of zonal wind shears within Saturn's troposphere when compared to cloudtop movements measured in reflected sunlight. For Titan, initial results include (1) the first detection and mapping of thermal emission spectra of CO, CO_2, and CH_3D on Titan's nightside limb, (2) the mapping of CH_4 fluorescence over the dayside bright limb, extending to ~750 km altitude, (3) wind measurements of ~0.5 ms^{-1}, favoring prograde, from the movement of a persistent (multiple months) south polar cloud near 88° S latitude, and (4) the imaging of two transient mid-southern-latitude cloud features.

1. Introduction

We report here initial results for the atmospheres of Saturn and Titan from observations by the Visual Infrared Mapping Spectrometer (VIMS) onboard the Cassini orbiter. VIMS is a multi-channel mapping spectrometer, which simultaneously acquires 352 bandpasses ranging from 0.35 to 5.1 μm (cf. Brown et al., 2004). The visible spectral range is mapped with the visual channel of the instrument, and is comprised of 96 contiguous bandpasses from 0.35 to 1.0 μm, with a spectral sampling interval of 0.006 μm. The near-infrared channel maps 256 contiguous bandpasses from 0.85 to 5.1 μm, with a spectral sampling interval of 0.016 μm. Spatially, these two channels each typically map a scene up to 32 mrad by 32 mrad across using internal mirrors. The visual channel maps one dimension along the columns of its two-dimensional CCD array (with spectra being acquired along the rows). The second spatial dimension is acquired with an internal mirror. The near-infrared channel is effectively a single-element, 256-channel spectrometer, which then maps spatially in two dimensions using two orthogonally directed mirrors. Both channels nominally produce spectral images with an IFOV (internal field-of-view) of 0.5 mrad by 0.5 mrad.

The integration time of the near-infrared channel is user-specified over a typical range of 20 to 1000 ms. Typically, the integration time of the visual

channel is coordinated with the near-IR channel, so that both observations are completed nearly simultaneously.

To achieve various science objectives for Saturn and Titan, several observational modes are possible (cf. Baines et al., 1992; Brown et al., 2005). For example, in the near-IR channel, narrowing the image size to 2×2 pixels and short integration times (e.g., 20 ms), stellar occultations can be effectively observed. Solar occultations can be observed as well in the near-IR through a solar port specifically designed for that purpose.

By far, nadir imaging is the primary mode of operation, encompassing more than 98% of the observing time for Saturn and Titan. Spectral mapping of Saturn and Titan can be obtained on both the day and night sides, with the integration times adjusted appropriately to enhance signal-to-noise without over saturating the detector. The wide spectral range enables simultaneous observations of a wide variety of atmospheric species, in both absorption of sunlight and in emission. The nature of hazes and cloud structures and the microphysical properties of aerosols within them can be deduced from the wavelength-dependent behavior of aerosol layers observed in sunlight over a variety of observing and solar incidence angles. For Saturn, valuable additional information on cloud and haze opacities and microphysical properties comes from 5-μm observations of the extinction of upwelling thermal radiation generated at depth. Repeated observations of cloud features over time provide measurements of dynamics, while measurements over phase angle provide constraints on particle phase functions.

In this paper we present initial results of nadir observations of Saturn and Titan, focusing on observations made with the near-IR channel. We present initial results from observations obtained with a variety of flux sources, including solar illumination observations, thermal emission maps and spectra, and CH_4 fluorescence.

2. Results

2.1. Spectra

As observed by VIMS, both Saturn and Titan exhibit rich near-infrared spectra (cf. Figure 1). Shortward of 4 μm, CH_4 is the dominant atmospheric absorber. Saturn has significant additional gaseous absorption due to ammonia and hydrogen, the latter dominating the 2.0–2.2 μm region with its strong 1–0 band pressure-induced absorption features. Near 5 μm, none of these prevalent gases effectively absorb, leaving a spectral emission window where radiant heat generated at depth can escape. As this internally generated upwelling flux encounters phosphine (PH_3), germane (GeH_4), carbon monoxide (CO), and deuterated methane (CH_3D) water, some of the

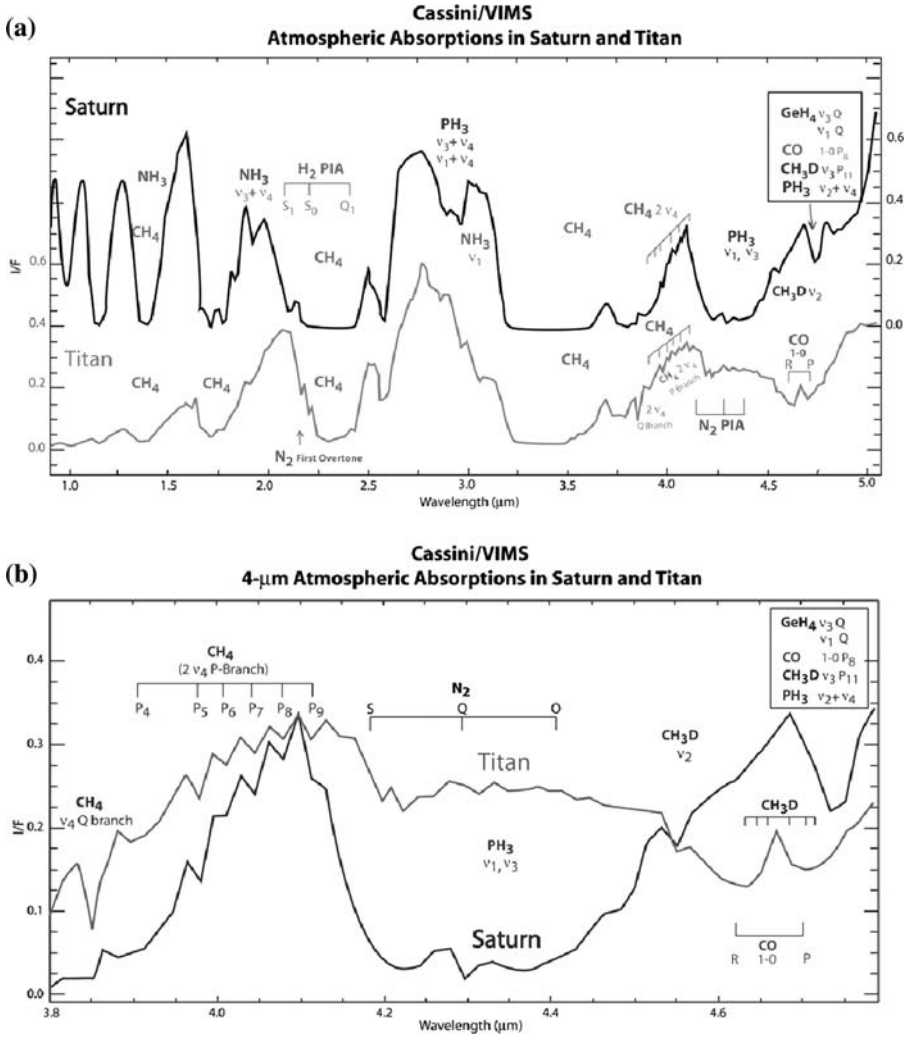

Figure 1. Near-IR atmospheric absorption spectra of Saturn and Titan, 1.0– 5.0 μm. Panel (a) Full spectra of Saturn (right I/F scale) and Titan (left scale). The Titan spectrum (CM 1477516605), obtained on October 26, 2004, is a medium-spatial-resolution (~55 km IFOV) high-phase-angle observation (166.7°) and is thus a long pathlength, pure spectrum of atmospheric absorption, uncontaminated by surface reflectance. Methane is the chief absorber on both Saturn and Titan. For Saturn, absorptions due to hydrogen, ammonia, and phosphine are also important. For Titan, CO absorptions are present near 4.7 μm. Panel (b) Near-IR spectra from 3.8 to 4.8 μm. Specific P branch lines for CH_4 $2\nu_4$ are depicted near 4.1 μm. The P and R branches of CO are clearly seen on Titan near 4.7 μm. The ν_2 feature of CH_3D is seen near 4.55 μm in both Saturn and Titan. Absorptions due to disequlibrium species phosphine, germane, and CO are seen near 5 μm. The Saturn spectrum is from VIMS observation CM 1465898991, taken on June 14, 2004, at a phase angle of 67.1° at a range of 9.97 million km from Saturn's clouds. The long integration times (160 ms) ensure a high S/N greater than 400:1 throughout the bulk of the spectra.

flux is absorbed, producing spectral features which thus reveal the presence of these trace species. The first three are disequilibrium species, meaning they are intrinsically short-lived in the planet's upper troposphere and stratosphere. Their presence indicates upwelling of material from below, from at least as deep as their formation range near 1000 km depth (e.g., Lewis and Fegley, 1984; Fegley and Prinn, 1985). Phosphine absorption is also observed near 2.95 μm on Saturn, as recently measured in the laboratory by Butler et al. (2005). CH_3D is an indicator of Saturn's origin. When compared with the abundance of CH_4, the derived D/H ratio is a key constraint on the origin of material which formed Saturn (e.g., comets falling in from the Kuiper Belt region). On Titan, additional absorptions near 4.65 μm are due to atmospheric carbon monoxide (CO), for which the envelope of both the P and R branches can be clearly seen. Near 4 μm, both the planet and its moon show a host of individual spectral features from the $2\nu_4$ P branch of methane.

2.2. Saturn clouds

VIMS images confirm the well-known zonal morphology of Saturn's cloud systems (cf. Figure 2). The most apparent clouds cover a broad (>20° of latitude) region surrounding the equator. These clouds extend to higher altitudes than others, as evidenced by their bright appearance in deep pressure-induced hydrogen and CH_4 absorption bands (e.g., 2.12 μm H_2 absorption image, Panel (a) of Figure 2). Another zonal feature is at 50° S latitude, and either lies deeper than the Equatorial Region (ER), or is comprised of substantially less 2.12-μm reflective material. However, a near-continuum image at 1.59 μm (b), indicates nearly uniform reflectivity across the disk, and strongly suggests that the inherent reflectivity of cloud material at 2.12 μm should be uniform as well. Thus, the spatial variability seen in the H_2 absorption band at 2.12 μm (and, indeed, at other absorbing wavelengths) is primarily due to variations in the vertical distribution of cloud material. In particular, this variability is largely due to variations in the altitudes of the tops of the highest clouds.

The morphology of clouds at 5 μm is distinctly different (cf. Figure 2(c)). Here, the dominant lighting is from internally generated thermal emission, not the Sun. Indeed, the nightside of Saturn is shown on the left-hand side of the disk in this image, and is nearly as bright as the dayside on the right. As first recognized in ground-based dayside observations of Yanamandra-Fisher et al. (2001), instead of a gross axisymmetric structure of latitudinally varying brightness, the atmosphere viewed at 5 μm appears quite uniformly sprinkled with light and dark spots. This different morphology is particularly apparent in the color composite (Figure 2(d)), which shows little correlation of the 5-μm flux with the axisymmetric bands of flux seen in reflected sunlight

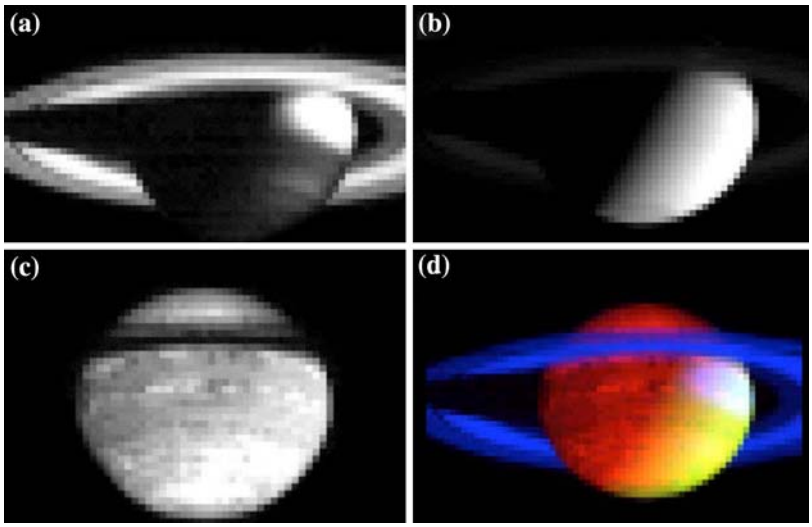

Figure 2. Saturn cloud morphology from near-IR maps. VIMS image cube CM1469259344 was acquired July 23, 2004, from 6.48 million km at a phase angle of 90.3°. The spacecraft is positioned over the morning terminator, with the sun to the right. Southern summer is seen, with the SPR completely sunlit. Panel (a) A broad band of equatorial clouds is relatively bright in 2.12-μm H_2 absorption, indicating a relatively high cloud altitude compared to clouds elsewhere. In contrast, at the 1.59 μm continuum wavelength (Panel b), the more constant brightness of Saturn across the disk shows that clouds are present virtually everywhere across Saturn. Panel (c) Observations at 5.1 μm show significant longitudinal structure. Here, clouds are seen as predominantly silhouetted against the thermal glow emanating from Saturn's deep, warm atmosphere. Thus, in contrast to images taken in reflected sunlight, here relatively bright areas are regions of relatively small cloud opacity, while relatively dark areas show regions of large opacity. The lack of significant organized latitudinal variability in 5-μm brightness compared to the zonally oriented brightness structures seen in reflected-solar wavelengths (cf. Panel d) indicates that the overlying solar-reflective zonally oriented clouds are comprised of relatively small, non-5-μm-attenuating particle.

at 2.12 μm and other H_2 and CH_2 absorption wavelengths. As we show below, these "cold" and "hot" spots are not thermal structures *per se*, but instead represent thick and thin clouds, respectively, which attenuate the upwelling 5-μm thermal emission to varying degrees. What this image indicates then is that at an atmospheric depth unobservable in sunlight, the clouds take on a discrete character, distinctly different from the canonical axisymmetric appearance of Saturn's sunlit clouds. The localized nature of these clouds suggests that vertical transport is more important in determining cloud morphology at these depths than at higher altitudes, perhaps causing cloud formation there via convection and/or vertical wave processes. The depth of this lower layer of discrete clouds is yet unconstrained. Likely possibilities include the bottom of the ammonia cloud layer near 1.3 bars, and the NH_4SH cloud layer near 4.2 bars, as predicted from ~7 times

enhancement over solar molar fractions of nitrogen and sulfur recently determined from Cassini/CIRS observations (Flasar et al., 2005a).

For the tops of the sunlit, optically thick axisymmetric clouds, quantitative altitude constraints can be determined from multispectral analysis. The basic procedure is to use a continuum wavelength – one not affected by absorption of atmospheric gases – to determine the single-scattering albedo of a presumably optically thick cloud. Since the atmosphere does not provide extinction (except perhaps by Rayleigh scattering, which is largely avoided with our choice of near-infrared wavelengths), the derived single-scattering albedo is not dependent on cloud altitude. With the derived single-scattering albedo, the next step is to analyze the brightness observed in a nearby wavelength which is affected by gas absorption. Using a wavelength where the vertical distribution of absorbing gas constituents are known (usually pertaining to a well-mixed constituent such as methane or hydrogen), the cloudtop brightness can be fit by varying the cloudtop pressure, using the previously established single-scattering albedo, under the assumption that (1) the clouds are optically thick, and (2) the cloud particle single-scattering albedo does not vary over the spectral range between continuum and absorption wavelengths. In this analysis, the phase function does not significantly affect the results, since all the data under analysis were taken simultaneously under the same lighting and observing conditions. Currently, we are performing such an analysis, extended to cover more realistic cases where the cloud opacity is not optically thick.

A limitation of this procedure is that as the cloudtop descends, eventually the atmospheric extinction is so great that the reflected cloudtop signal is weakened below the inherent noise level of the observations. At deeper levels, a weaker absorption wavelength capable of peering deeper into the atmosphere is needed to provide vertical constraints. Fortunately, the large range of methane and hydrogen absorption coefficients afforded in the near-infrared provides a means for VIMS to effectively determine cloudtop pressures over an extensive range of altitudes. As shown in Figure 3, in the absence of overlying clouds, cloudtop altitudes from the high stratosphere near 1 mbar down below the 10 bar level in the troposphere can be effectively probed with VIMS. In Figure 3, we show the level in the atmosphere where an optically thick, completely reflective cloud would be observed as reflecting back e^{-1} (0.368) of the incident sunlight impinging the top of the atmosphere, for a nadir geometry wherein both the sun and observer are directly above the reflecting cloud. The pressure-induced 1–0 H_2 band in the 2.0–2.2 μm range affords a particularly effective means of constraining cloud distributions in the 10 mbar to 0.4 bar range, while strong CH_4 absorptions at 2.2–2.4 μm constrain aerosols at high altitudes up to at least the 5 mbar level.

Thus, VIMS spectral imaging observations spanning a large range of wavelengths (0.3–5.1 μm) and atmospheric extinction strengths can be used to

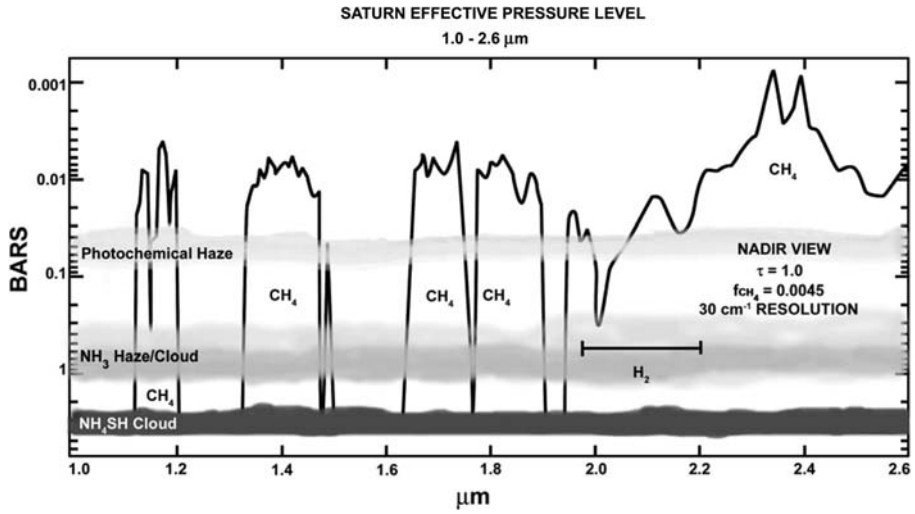

Figure 3. Saturn effective pressure levels from 1– 2.5 μm. The depth at which atmospheric gas opacity reaches unity for a two-way nadir path is depicted as a function of wavelength. The depths of cloud and haze layers can be effectively constrained over four orders of magnitude of pressures in this spectral region. Here, the correlated-K approach (Goody et al. 1989; Lacis and Oinas 1991) is used to determine the effective CH_4 gas opacity, using CH_4 absorption coefficients of Baines et al. (1993) interpolated for the temperature/pressure structure of Saturn given a CH_4 mixing ratio of 0.0045 after Courtin et al. (1984). The pressure-induced hydrogen absorption near 2 μm was calculated using the formalisms of Borysow (1992). The location of the NH_3 cloudbase is from Tomasko et al. (1984). The NH_4SH cloud-base is at 4.2 bars, assuming nitrogen and sulfur are enhanced by a factor of seven compared to their solar elemental abundances, as indicated by recent Cassini/CIRS measurements (Flasar et al., 2005a).

quantitatively determine meaningful constraints on the vertical structure of features across the planet. The evolution of these structures over several years can also be quantitatively evaluated. As well, constraints on haze and cloud phase functions can be assessed from the variety of phase angles sampled over a wide range of non-gas-absorbing wavelengths by the orbiting Cassini spacecraft. Such in-depth multi-spectral quantitative analyses of cloud structures is the subject of ongoing studies and is beyond the scope of this survey paper. Here, we now present early results on atmospheric structure derived from the qualitative aspects of the data, including evidence of spatial variabilities in the abundances of the trace gases, phosphine and ammonia.

2.3. Evidence for depletion of phosphine in southern belts

The dual simultaneous instrumental capabilities of (1) two-dimensional spatial mapping and (2) extensive spectral coverage, together enable VIMS to

efficiently map a variety of atmospheric constituents over the planet. Here and in the next section we use these capabilities to present evidence that (1) phosphine is depleted in less cloudy belts relative to the more cloudy ER, and (2) absorptions by phosphine, ammonia, methane, and hydrogen are all unusually strong in the South Polar Region (SPR), not inconsistent with the relatively deep clouds observed there.

As discussed earlier and shown in Figure 1, CH_4, H_2, NH_3, and PH_3 all absorb at VIMS wavelengths. Figure 4 shows the near-infrared spectra for the ER and the nearby southern temperate belt (STeB). The spectra look similar in overall shape. The main difference is that the belt absorbs significantly more at H_2 and CH_4 absorption wavelengths, as seen more clearly in the ratio of these two spectra shown in Figure 4(c). As noted earlier, such a behavior in these well-mixed gases can be readily attributed to variations in cloud structure. In this case, the STeB cloudtops are found to reside at significantly deeper levels than the ER clouds.

Ammonia also absorbs more in the STeB than in the ER, as indicated in the enhanced absorption seen near 1.99 μm. This, too, can be explained by the increased depth of view allowed in the STeB due to the decreased cloudtop altitude.

Phosphine behaves differently. Contrary to the behavior of methane, hydrogen, and ammonia, absorption by phosphine is nearly identical in these two regions. This is readily seen in the ratio spectrum (Figure 4(c)), where the ratio is flat throughout the phosphine absorption complex from 2.75 to 3.0 μm. This difference in behavior strongly indicates that the vertically averaged PH_3 mixing ratio above the cloudtops is significantly less in the STeB than in the ER. Since PH_3 is a disequilibrium species formed at high temperatures (~1000 K) deep in the atmosphere and readily destroyed in the cold, observable atmosphere by both cold-temperature chemical and photolytic processes in ~100 days (e.g., Atreya, 1986), this suggests that vertical transport of PH_3 from the interior is significantly less in the STeB than in the ER. This in turn is strong evidence for enhanced upwelling from depth in the ER vs a nearby belt.

A similar behavior is seen in the southern polar belt (SPB) located near 56.3° S latitude (cf. Figure 5). Again, enhanced absorptions of the well-mixed constituents CH_4 and H_2 are clearly seen in the ratio spectrum (Panel c). These increased absorption are due to the increased pathlengths caused by (1) the larger solar incidence and viewing angles for the southern belt (2) and, perhaps, deeper cloudtops there. However, PH_3 absorptions near 2.8 and 4.75 μm are not similarly enhanced, thus indicating that phosphine may be relatively depleted in the southern belt relative to the ER, and thus upwelling from depth is likely greater in the ER. This behavior of belts vs brighter zones is not unexpected, as neighboring Jupiter exhibits a similar nature. There, bright zonal features appear to be regions of relative upwelling, with higher,

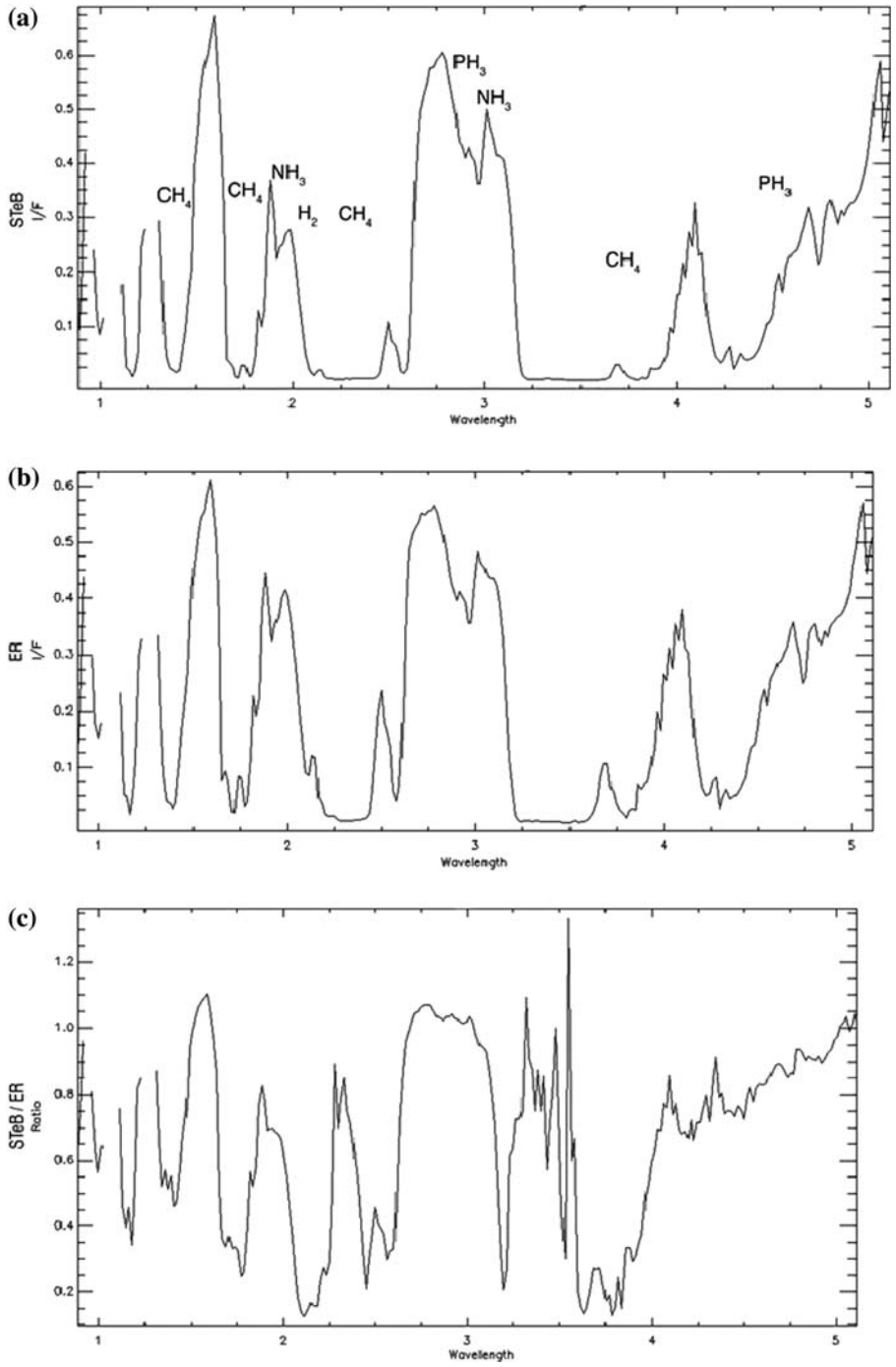
(a)
STeB I/F
CH4
CH4
NH3
H2
CH4
PH3
NH3
CH4
PH3
Wavelength
(b)
ER I/F
Wavelength
(c)
STeB / ER Ratio
Wavelength

Figure 4. Spectra of south temperate belt (STeB, observed here at 27.9° S latitude, Panel (a) and ER (1.5° S latitude, Panel (b)). In addition to CH_4 and H_2 absorptions, prominent absorptions due to PH_3 near 2.8 and 4.2–4.9 μm are depicted in both the STeB and ER spectra. The band depths of these PH_3 features are comparable in both spectra, as illustrated in the ratio spectrum (Panel c) showing relatively flat spectral signatures for PH_3. On the other hand, the H_2 pressure-induced absorption near 2.1 μm, the CH_4 absorptions near 3.8–4.0 μm, and the ammonia band absorption near 1.99 μm are all deeper in the STeB spectrum, leaving marked signatures of these species in the ratio spectrum. The fact that the phosphine absorption does not similarly increase between the ER and STeB indicates that phosphine may be relatively depleted in the STeB relative to the ER. Spectra are from VIMS observation CM1472983590, acquired on September 4, 2004 from a distance of 9.0 million km at a phase angle of 84.5°. The spectra shown here are from the minimum air mass point at the specified latitude, at a relative longitude of 42° on the sunlit side, to minimize the aerosol and gas extinction per km altitude and provide the deepest views of the atmosphere.

thicker condensation clouds and trace species vapor abundances (such as ammonia), while darker belts appear to be regions of relative subsidence (e.g., Ingersoll et al., 1984; Baines et al., 1989).

2.4. Evidence for relative enhancement of absorptions by phosphine and ammonia in the SPR

In contrast to the relative depletion of phosphine observed in the two belts discussed above, the SPR shows distinct enhancements in the column abundance of phosphine. As shown in Figure 6, the spectral ratio of the SPR relative to the ER shows additional 2.9- μm and 4.7- μm PH_3 absorption near the pole. A similar enhancement occurs for the ammonia absorption at 1.99 μm. The spatial extent of these enhancements are depicted in Figure 7. Here, in the right-hand panels, we show the continuum-to-absorption brightness ratios for the two phosphine bands and one ammonia band. In all three cases, this ratio is increased by over 40% southward of approximately 65° S latitude, indicating relative enhancements in column absorptions for both phosphine and ammonia.

These absorption enhancements appear to be well correlated with cloud structure, as shown in the color images of Figure 8. Here, blue is used to depict the continuum-to-absorption brightness ratios, while red and green denote cloud brightnesses as mapped in the continuum wavelengths at 1.59 and 1.89 μm. In the SPR, the cloud brightnesses fade significantly, while the continuum-to-absorption brightness ratios increase, resulting in a distinctly bluish coloring to the SPR. The fading of the clouds there may be due to both a thinning of the cloud opacity as well as the lowering of the cloudtop to deeper depths. This is suggested by Figure 8(d), where we show only

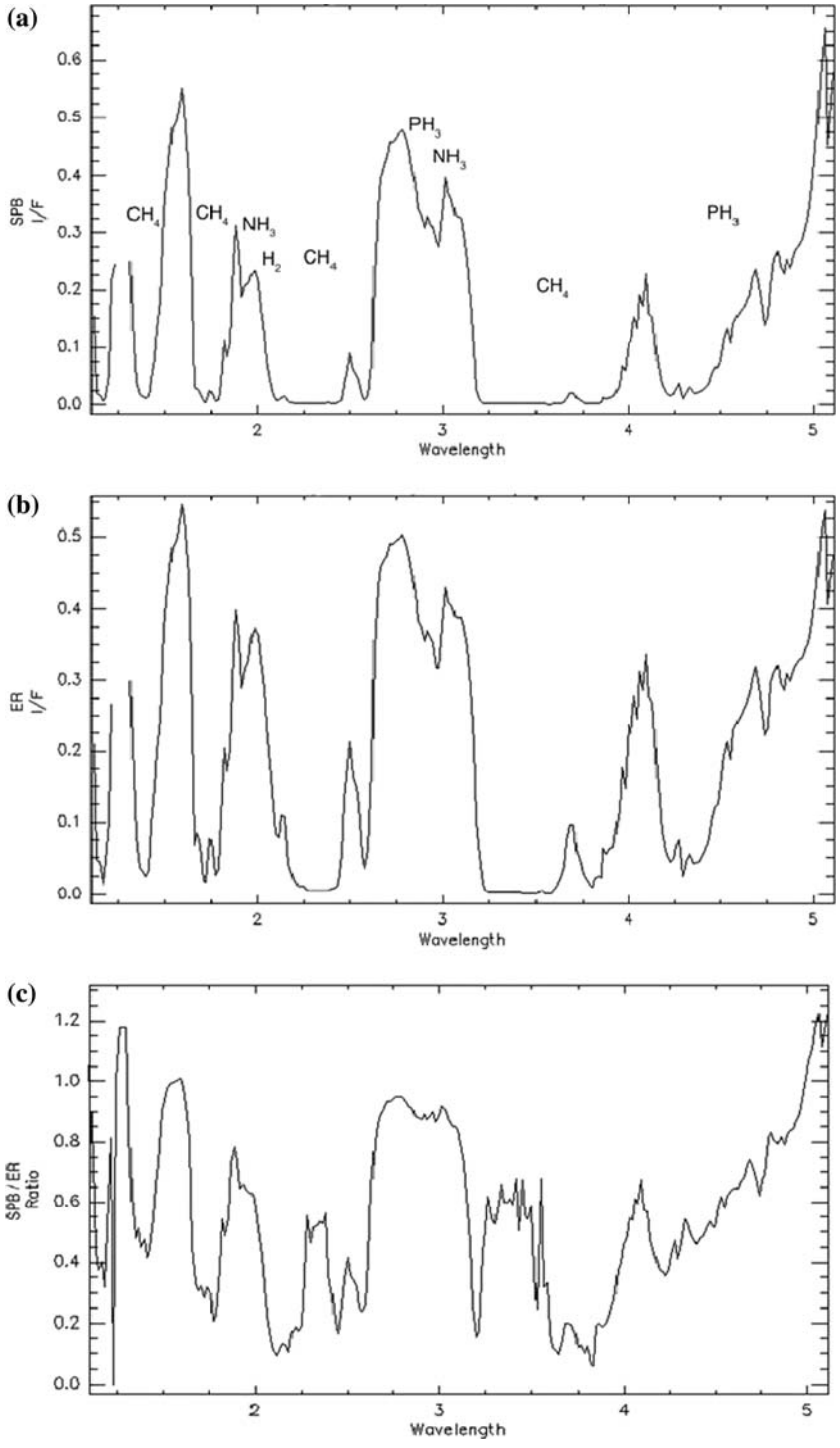
(a)
SPB I/F
CH4
CH4
NH3
H2
CH4
PH3
NH3
CH4
PH3
Wavelength
(b)
ER I/F
Wavelength
(c)
SPB / ER Ratio
Wavelength

Figure 5. Spectra of SPB (56.3° S latitude) and bright ER (1.5° S latitude). As in Figure 4, compared to the ER (Panel b), the darker belt region (Panel a) exhibits enhanced absorptions of the well-mixed constituents CH_4 and H_2 – as clearly shown in the ratio spectrum (Panel c) – due to increased pathlengths perhaps caused by the deeper cloudtops and larger solar incidence and viewing angles for the belt. However, absorptions due to PH_3 near 2.8 and 4.75 μm are not similarly enhanced in the southern belt – as evidenced by the subdued PH_3 signature seen in Panel (c) – thus indicating that phosphine may be relatively depleted in the southern belt relative to the ER. Spectra are from VIMS observation CM1472983590, acquired on September 4, 2004 from a distance of 9.0 million km at a phase angle of 84.5°. The spectra shown here are from the minimum air mass point at the specified latitude, at a relative longitude of 42° on the sunlit side, to mimimize the aerosol and gas extinction per km altitude and provide the deepest views of the atmosphere.

cloud properties. Specifically, here we use blue to denote cloudtop altitude via the reflectivity observed in H_2 absorption at 2.08 μm. Due to the evidently lower-lying and less-reflective clouds there, the clouds appear a brownish color, instead of the bright yellows and whites depicted at non-polar latitudes. This variation in vertical cloud distribution may be responsible for the enhanced PH_3 and NH_3 absorptions seen in Panels (a)–(c). Specifically, the observed enhancements in trace gas absorptions may be due to the increased air mass sampled above the cloud reflectors in the SPR and not due to intrinsic variabilities in the relative abundances of trace constituents there.

Latitudinal profiles of brightness ratios and cloud reflectivities are shown in Figure 9. Poleward of 60° S latitude, phosphine absorptions near 2.97 and 4.75 μm are enhanced by 30% and 60%, respectively, over temperate latitudes (solid and dashed curves in Panel (a), showing 2.79/ 2.97 and 4.68/ 4.75 μm brightness ratios, respectively). The ammonia absorption is also enhanced, by 45% (Panel (c), showing 1.89/1.99 μm brightness ratio). These enhancements coincide with changes in the latitudinal cloud structure, as indicated by the sharp polar decrease in reflectivity observed in the latitudinal profiles of both continuum and H_2 absorptions, here represented by the 1.59- μm continuum (Panel d) and shoulder of the 1–0 S(1) H_2 pressure-induced-absorption (2.03 μm in Panel (e), 2.08 μm in Panel f). Thus it is far from certain that the increased absorptions in the non-uniformly mixed gases phosphine and ammonia represent polar enhancements in the molar fractions of these substances. Rather, the increased column abundances and air mass above the deeper reflecting cloud layers there may explain the enhanced absorptions. Quantitative modeling is presently underway to definitively evaluate the mixing ratios of these gases over the visible disk.

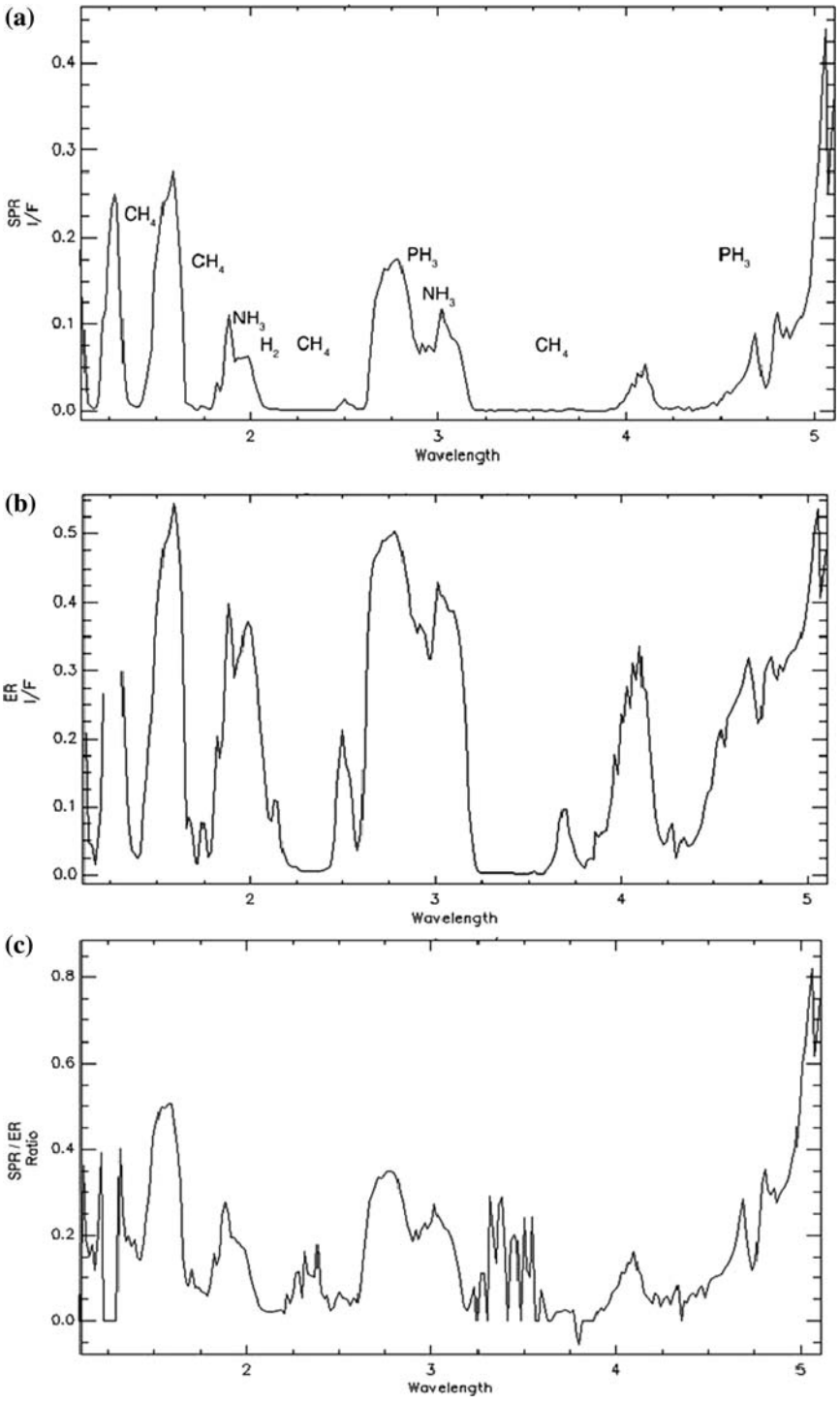
(a)
SPR I/F
CH4
CH4
NH3
H2
CH4
PH3
NH3
CH4
PH3
Wavelength
(b)
ER I/F
Wavelength
(c)
SPR/ER Ratio
Wavelength

Figure 6. Saturn spectra: The SPR (83.2° S latitude, Panel (a) vs the ER (5.0° S latitude, Panel (b)). Prominent PH_3 absorptions are distinctly different in the two spectra, as shown in the ratio spectrum of the SPR spectrum divided by the ER spectrum (Panel c). Here, the enhanced phosphine absorption in the polar region is seen as a mimicking of the polar spectrum itself at both 2.8 and 4.7 μm. This spectral behavior is in distinct contrast to the nearly flat ratio across these spectral features obtained for both the 27.9° S latitude STeB and the 56° south latititude SPB, ratioed to the bright ER shown in Panel (c) of both Figures 4 and 5. Spectra are from VIMS observation CM1472983590, acquired on September 4, 2004 from a distance of 9.0 million km at a phase angle of 84.5°. The spectra shown here are from the point of minimum air mass at the specified latitude, at a relative longitude of 42° on the sunlit side, to minimize the aerosol and gas extinction per km altitude and provide the deepest views of the atmosphere.

2.5. Saturn CH_4 fluorescence

Figure 10 shows spatially resolved 3.32 μ-m CH_4 fluorescence on Saturn, as first mapped by VIMS. CH_4 fluorescence is created by the non-LTE scattering of solar light absorbed by methane within one of its vibrational levels and re-emitted before collisional damping can occur. Disk-integrated fluorescence has been previously observed by ISO/SWS (Drossart et al., 1999). Since the relevant weighting functions are phase-angle dependent, views over a variety of phase angles unavailable from Earth – such as the view in Figure 10 at 85° phase – enable increased accuracy in the determinations of mesospheric CH_4 abundances and the eddy diffusion coefficient near the homopause. VIMS is the first instrument to spatially map this fluorescence. It can thus determine the eddy diffusion coefficient over latitude, thereby further illuminating dynamical processes in the upper mesosphere. A detailed analysis of such images is presently underway for publication in the near future.

2.6. Saturn backlit clouds at 5 μm

At 5 μm, Saturn's clouds are predominantly backlit, as demonstrated in Figure 11 which simultaneously shows both the day and night sides of the planet. In this image at 87° phase angle, the dayside and nightside differ by less than a factor of two. This is particularly evident in the longitudinal profile plot (Panel d) at 46° S latitude, where the central meridian crosses the terminator, so that the nightside and dayside each occupy half the profile. Reflecting the nightside half of the profile over the central meridian onto the dayside, we see that the sunlit brightness exceeds the nightside brightness by about half the nighttime flux. Thus, at this phase angle, roughly 2/3 of the observed 5-μm daytime flux comes from thermal radiation, while 1/3 comes from reflected sunlight.

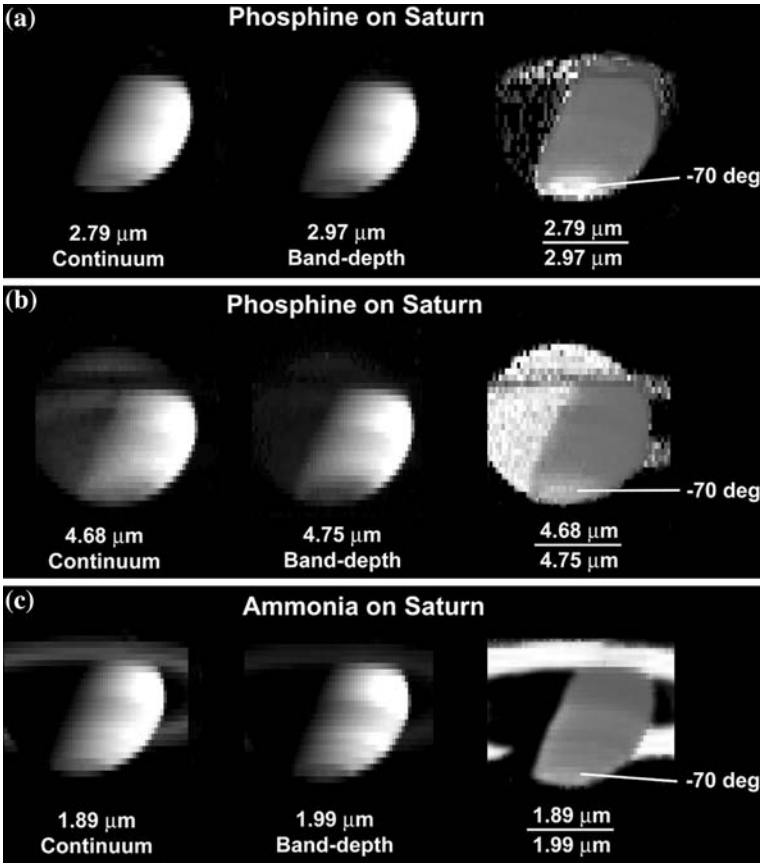

Figure 7. Maps of enhanced phosphine and ammonia absorption in the SPR. Ratios of continuum to absorption brightnesses are shown for two phosphine absorption regions (rows a and b) and an ammonia absorption (row c). Contrast in strong phosphine-absorbing wavelength of 2.97 μm is significantly greater than in the pseudo-continuum wavelength, 2.79 μm (row a). The brightness ratio $I/F_{2.79}/I/F_{2.97}$ is enhanced by more than 20% in the SPRs south of 70° S latitude vs equatorial and temperate latitudes. The contrast enhancement in the PH_3, GeH_4, CO, CH_3D complex at 4.75 μm is greater, with a ~40% increase in the $I/F_{4.68}/I/F_{4.75}$ brightness ratio (row b) in the polar region. For ammonia, contrast enhancement at the south pole is also observed (row c), for the $I/F_{1.89}/I/F_{1.99}$ brightness ratio (bottom row). Images are from VIMS observation CM1472983590, acquired on September 4, 2004 from a distance of 9.0 million km at a phase angle of 84.5°.

We find that the point-to-point spatial variability in nightside flux comes predominantly from variations in cloud transmissivity/opacity, not local temperature. Figure 11(c) depicts a longitudinal profile at 8° S latitude, showing peak/minimum flux ratios greater than two over small spatial scales less than 5000 km. This corresponds to an extinction in tropospheric cloud opacity of ~0.8, quite plausible given the opacity variations observed

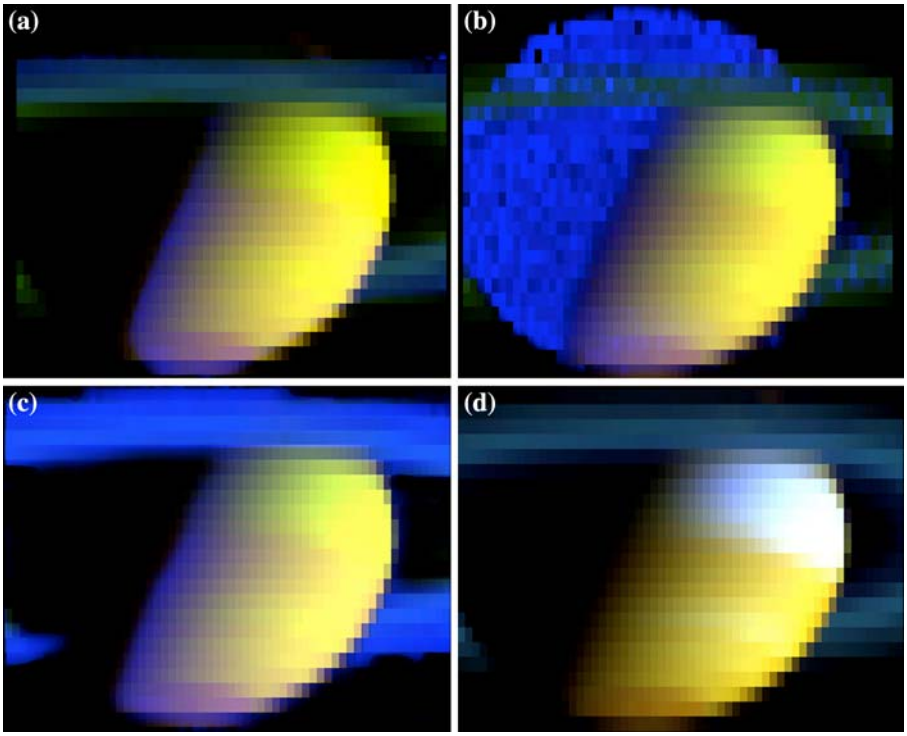

Figure 8. South polar enhancements of phosphine and ammonia absorptions compared with cloud variability. In each color image, cloud reflection in two pseudo-continuum, essentially non-absorbing wavelengths, 1.59 μm and 1.88 μm, are depicted by red and green, respectively. Trace gas absorption strengths, represented as brightness ratios of pseudo-continuum-to-absorption fluxes as in Figure 7, are depicted as blue in Panels (a)–(c) (Panel a: 2.79/2.97 μm; Panel (b) 4.68/4.75 μm; Panel (c) 1.88/1.99 μm). In each case, polar enhancement is seen as a distinct bluish haze. The relative lack of red and green there indicates a correlated decrease in cloud reflectivity, as emphasized in Panel (d), where blue is represented as an H_2 absorption wavelength, 2.08 μm. South polar clouds appear a dark brownish color, instead of the bright yellows and whites depicted at non-polar latitudes, indicating less reflective, relatively low-lying clouds there. This variation in vertical cloud distribution may be responsible for the enhanced PH_3 and NH_3 absorptions seen in Panels (a)–(c).

at 5-μm in Saturn's neighbor, Jupiter (e.g., Ortiz et al., 1998). Alternatively, ascribing this factor-of-two variability in flux to temperature variations leads to 50 K spatial variability on 5000-km scales. This is more than an order of magnitude greater than the observed mean equator-to-pole variability seen in our images, and certainly not dynamically consistent with the steady, axisymmetric, zonal winds measured over the decades in sunlit tracked features (e.g., Smith et al., 1981, 1982; Ingersoll et al., 1984; Sanchez-Lavega et al., 1999), nor by these thermally lit features themselves, as we now discuss.

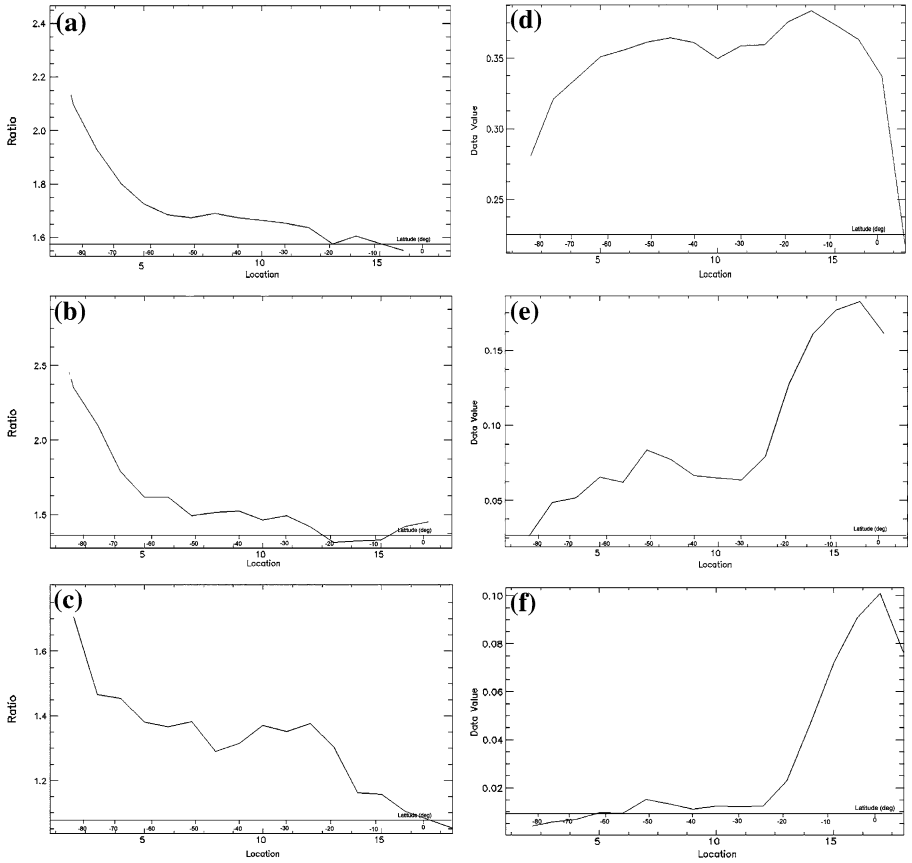

Figure 9. Latitudinal profiles of phosphine and ammonia absorption brightness ratios and cloud reflectivities. Absorptions by these two non-uniformly mixed trace species are enhanced poleward of ~65° S latitude. Phosphine absorptions near 2.97 μm (Panel (a), showing 2.79/2.97 μm brightness ratio) and 4.75 μm (Panel (b), showing 4.68/4.75 μm brightness ratio) are enhanced by >30% and >60%, respectively, at the pole compared to temperate latitudes. The ammonia absorption is enhanced by ~50% (Panel (c), showing 1.89/1.99 μm brightness ratio). These enhancements coincide with changes in the latitudinal cloud structure, as indicated by the sharp polar decrease in reflectivity observed in the latitudinal profiles of both continuum and H_2 absorptions, here represented by the 1.59-μm continuum (Panel d), and 2.03-μm shoulder and 2.08-μm near-peak of the 1–0 S(1) H_2 pressure-induced-absorption (Panels e and f, respectively).

2.7. Saturn winds from tracking of backlit clouds

Thermally backlit clouds are particularly useful for measuring Saturn's windfield. Due to (1) their localized, discrete nature (as contrasted to the zonally homogeneous appearance of clouds viewed only in reflected sunlight), (2) their ready identification on both dayside and nightside images, (3) their

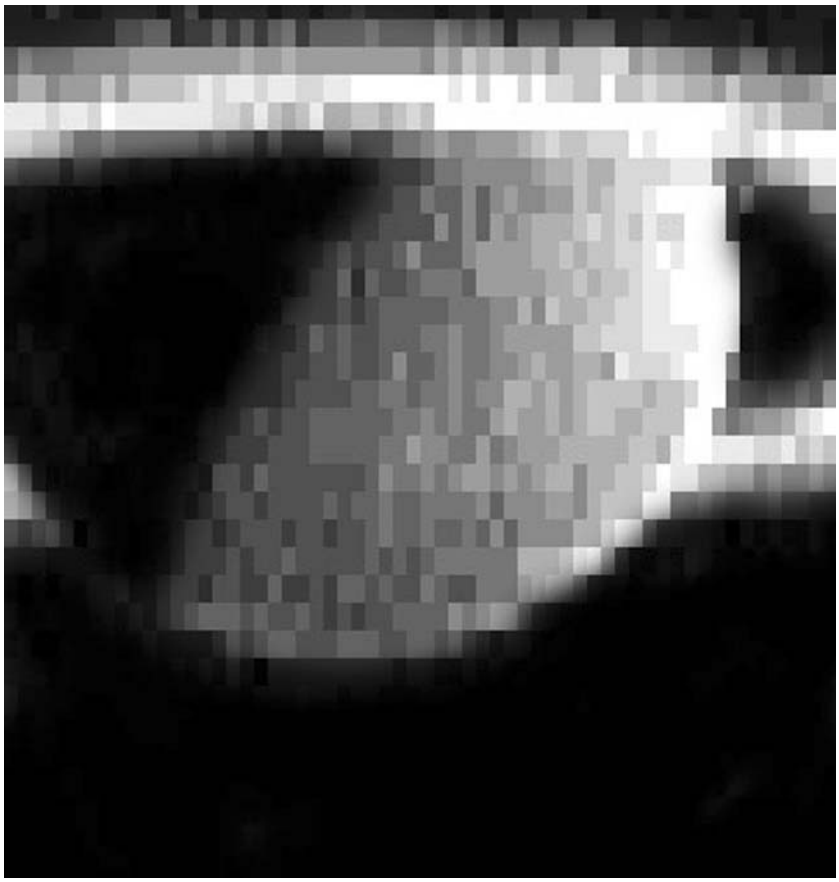

Figure 10. Methane fluorescence on Saturn. Brighter pixels concentrated at the limb show relatively strong fluorescence, due to the increased pathlengths per pixel there due to near-optimal observational and solar incidence angles. Image is from VIMS observation CM1472983590, acquired on September 4, 2004 from a distance of 9.0 million km at a phase angle of 84.5°. Integration time is 240 ms.

persistence over many days, and (4) the relatively low altitude of cloud extinction, these features offer a unique and accurate means to measure winds at depths deeper than measured heretofore. In Figure 12, we show images acquired each (Earth) day for 5 days. The persistence of spots can be seen, as demonstrated by the two bright features (arrows), which represent clearings between persistent cloud features.

Preliminary measurements of such features indicate zonal windspeeds of $\sim 390 \pm 50$ m s^{-1} at 8° S latitude in the ER. This is consistent with past Voyager measurements of winds in the ER by Smith et al., 1982 and Ingersoll et al. (1984), but inconsistent with the more recent wind measurements of ~270 m s^{-1} obtained by Sanchez-Lavega et al. (1999). Since these measurements are at a deeper depth than previously reported, any differences

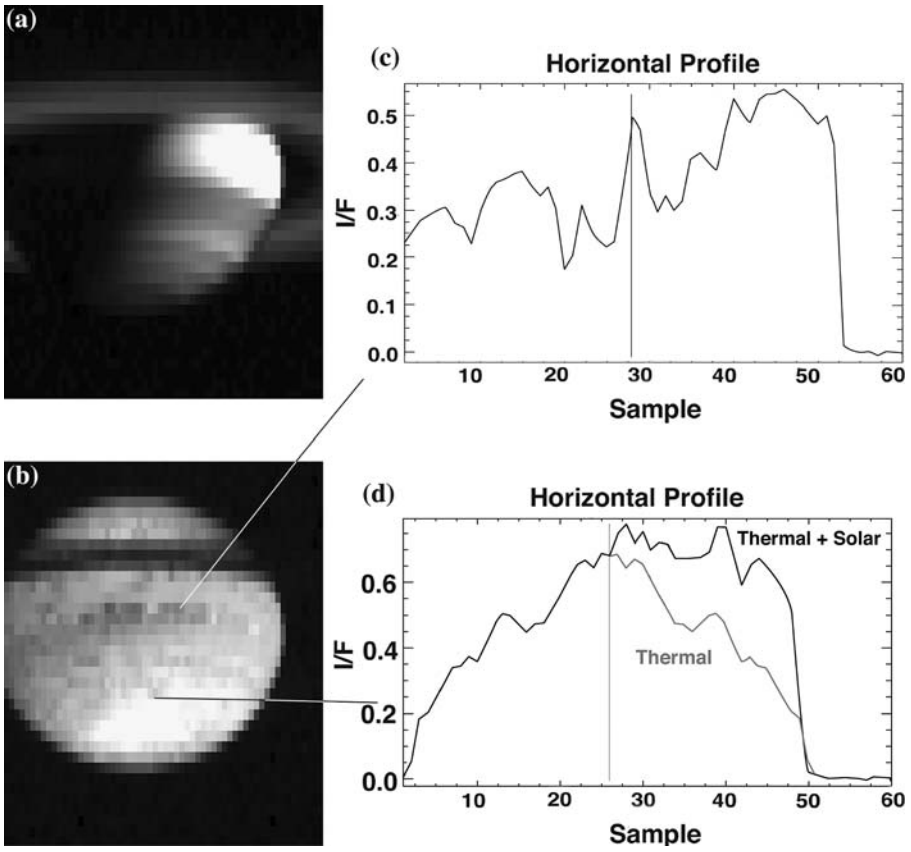

Figure 11. Contrasting views of Saturn, in reflected sunlight at 2.07 μm (Panel a) and illuminated by Saturn's thermal flux at 5.11 μm (Panel b). Zonal features are prominent in reflected sunlight, while localized, discrete cloud features dominate the 5-μm scene. Silhouetted against Saturn's 5-μm bright thermal radiation upwelling from depth, thick clouds are seen as relatively dark features (Panel b). Across the disk, point-to-point contrasts exceeding 80% are observed (see longitudinal profile for 8° S latitude, Panel c), indicating significant spatial variability in cloud opacity. On the dayside of this 5-μm image, reflected sunlight provides significant additional flux, as depicted in the lower right part of this 90° phase image and quantitatively in Panel d. Here, the nighttime flux at 46° S latitude is shown reflected over the terminator onto the dayside. About 1/3 of the daylight 5-μm flux is due to reflected sunlight. Images from VIMS observation CM1472983590, acquired September 5, 2004 from a distance of 8.936 million km at a phase angle of 84.5°. The IFOV at the center-of-disk is 4500 km.

between our measurements and others – all of which were taken with reflected sunlight near the cloudtops – may be due to vertical shear in the zonal windfield. To refine our analysis, we are continuing to analyze Saturn's windfield with newer data acquired at higher spatial resolution. As well, center-to-limb observations obtained in subsequent orbits will enable the

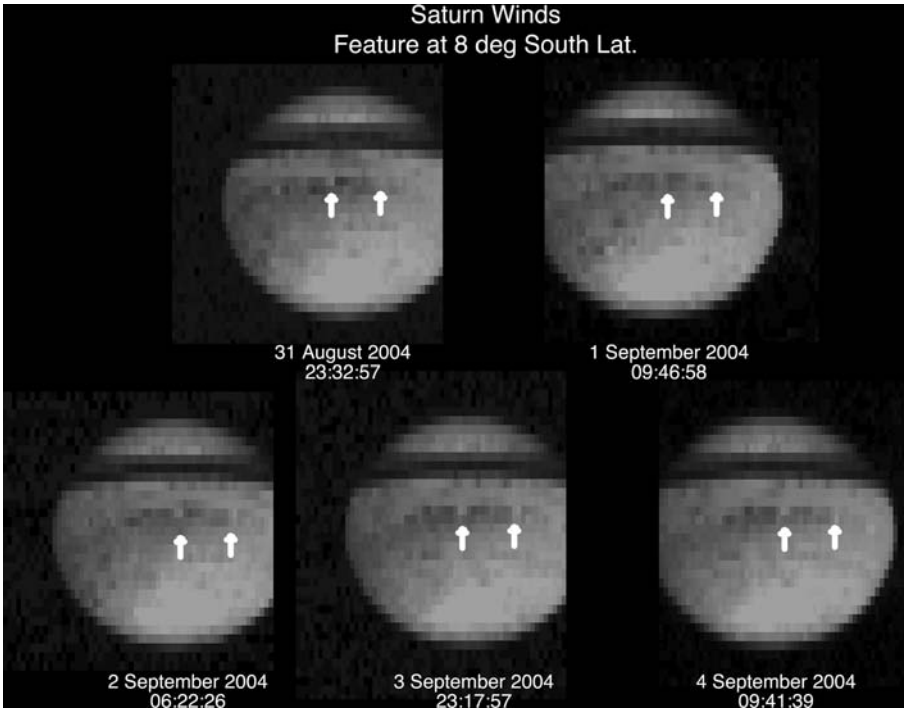

Figure 12. Saturn backlit-cloud tracking at 5 μm. Five images acquired over five (Earth) days are shown. At 8° S latitude, two bright features, representing cloud clearings (arrows), persist for the entire period, enabling effective measurements of the zonal wind. Images acquired from approximately 8.97 million km at a phase angle near 85°. Specific images and times are: (1) CM 1472684295 obtained 23:32, August 31, 2004 from 9.002 million km altitude above the 1-bar level at 85.5° phase, (2) CM 1472724707, 09:47 September 1, 2004 from 8.96 million km altitude, 85.4° phase, (3) CM 1472798836, 06:23 September 2, 1004, 8.981 million km altitude, 85.1° phase, (4) CM 1472946168, 23:27 September 4, 2004, 8.946 million km altitude, 84.7° phase, and (5) CM 1472983590, 09:41 September 5, 2004, 8.936 million km altitude, 84.5° phase angle.

detailed analysis of features necessary to better determine the altitude of our measurements. We also continue to look for discrete sunlit features that can be used to measure winds at higher altitudes, thus enabling a direct determination of vertical windshears. Another goal of such observations is to measure long-term temporal variabilities from direct comparison of new cloudtop winds measurements to previous Voyager and groundbased results.

2.8. Titan cloud-tracked winds

As predicted (e.g., Baines et al., 1992), VIMS is able to pierce through Titan's ubiquitous haze layer to obtain for the first time clear, high-resolution,

multi-filter images of Titan's surface and lower atmospheric clouds – including any surface fogs and cryovolcanic plumes. Indeed, the first VIMS observation at better than 2 km resolution revealed the presence of an unusual morphological feature on the planet's surface, suggested to be a cryovolcano (Sotin et al., 2005). The ability of VIMS to peer through the high-altitude mists of Titan is demonstrated in Figure 13. Due principally to the small size of Titan's haze particles (cf. Toon et al., 1992; Baines et al., 1992), aerosol extinction falls dramatically between 1 and 2 μm, thus enabling progressively sharper imaging of the surface over this spectral range. Such surface and deep-atmosphere imaging is possible only in discrete spectral "windows" in the near-infrared, where atmospheric absorption due to CH_4 gas is low. As shown in Figure 1, such near-infrared windows are located at

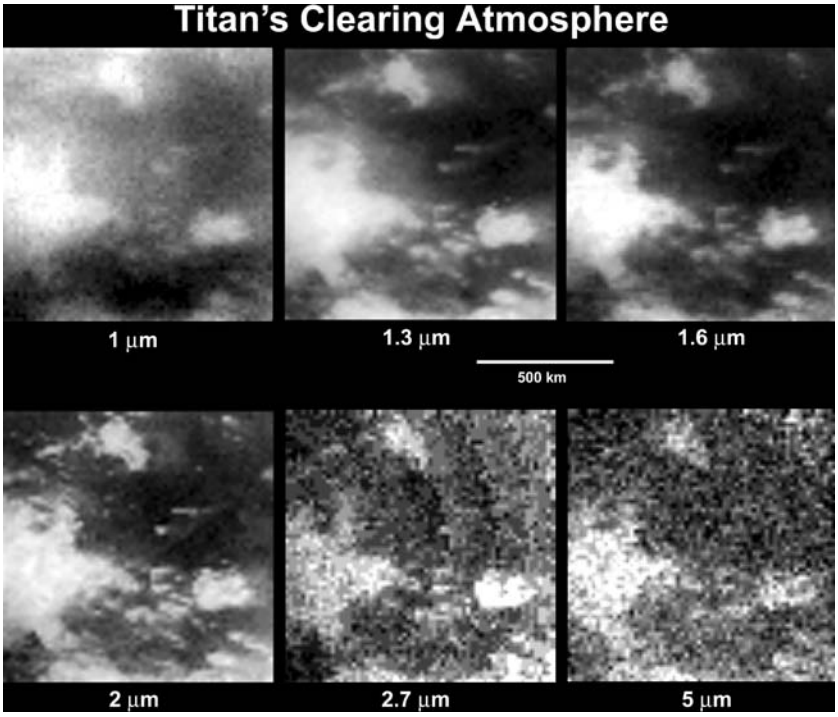

Figure 13. Clearing of Titan's atmosphere in the near-IR. Maps simultaneously acquired at 1.0, 1.3, 1.6, 2.0, 2.7 and 5.0 μm clearly show the dramatic improvement in surface visibility afforded in the near-infrared beyond 1.0 μm in non-methane-absorbing spectroscopic windows. VIMS observation CM 1477491859 was obtained October 26, 2004 from 0.0285 million km, corresponding to a VIMS IFOV of 14.3 km/pixel. Obtained at a low phase angle (13.7°), a small integration time (40 ms/pixel) was used to reduce smear due to spacecraft motions, thus ensuring preservation of the inherent IFOV-determined resolution. Images in the 2.7- and 5.0- μm windows are significantly noisier than the 2.0- μm image due to the relatively low levels of 2.7- μm surface reflectivity and 5- μm solar flux.

1.0,1.3, 1.6, 2.0, 2.7, and 5.0 μm. The 5-μm window is somewhat limited by poor signal-to-noise due to both the diminishing throughput of the VIMS instrument as well as the diminishing solar flux. However, this can be mitigated by (1) longer integration times or (2) co-adding of signal over adjacent wavelengths. The poor signal-to-noise observed in the 2.7 μm window is primarily due to the low reflectivity of the surface.

During Cassini's first encounter with Titan on July 2, 2004, four cloud features were observed in the SPR. As depicted in Figure 14, the most prominent cloud was observed near 88° S latitude, and was approximately

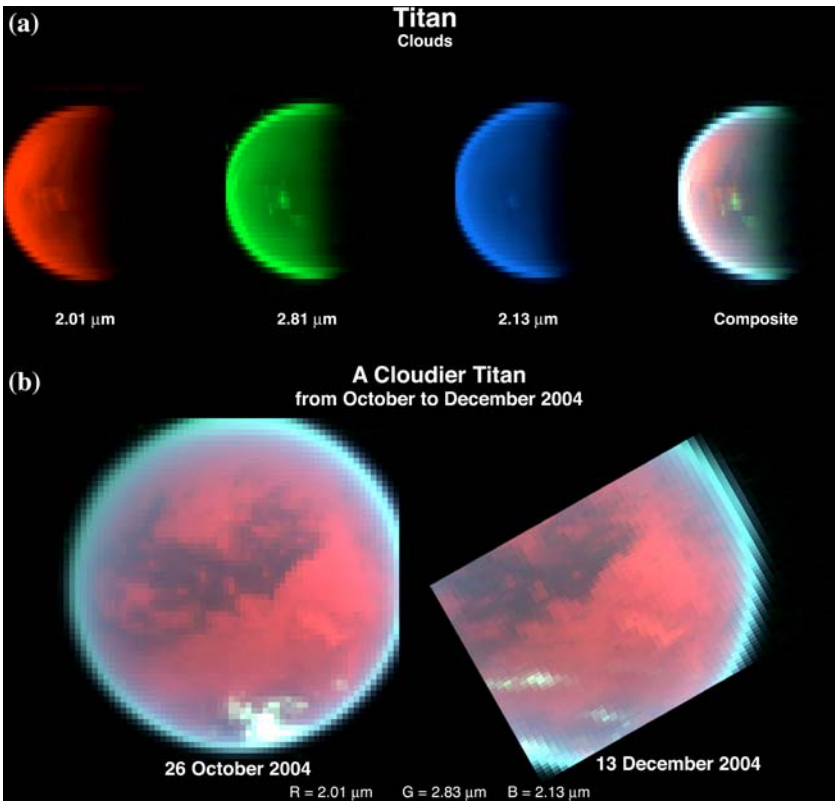

Figure 14. Titan clouds. Panel (a) South polar clouds on Titan observed on Cassini's first encounter with Titan, July 2, 2004 from a distance of 377.5 thousand km and a phase angle of 85.9° (VIMS observation CM1467473147), with the spacecraft located almost directly over the south pole. Four clouds are readily apparent at 2.01 μm (red) and 2.81 μm (green). The most prominent, poleward cloud at 88° S latitude is apparent in all of these false-color images, including a CH_4-absorbing wavelength near 2.13 μm (blue). Panel b: Titan cloud variability. Maps of the same face of Titan obtained 7 weeks apart show different distributions of clouds at southern mid-latitudes. The left image is from observation CM1477461989, obtained October 26, 2004 from 0.183 million km, at a phase angle of 13.2°. The right hand image was obtained December 13, 2004 from 0.224 million km at a similar phase angle of 15.0°.

700 km in diameter. The smaller clouds were all located within 6° of latitude of the major cloud, and ranged in size from 65 to 170 km in diameter. All four clouds are visible in the 2.01 and 2.81 μm methane windows, shown as red and green, respectively, in Figure 14, Panel (a). The prominent polar cloud is also visible at 2.13 μm, in CH_4 absorption, as shown in the blue image. Our initial modeling indicates it is located at approximately 30 km altitude above the surface. This cloud proved observable for 13 h on Cassini's first Titan encounter, enabling measurements of a zonal windspeed of 0.5 ± 3.0 m s^{-1}, slightly favoring a prograde motion, as discussed in Brown et al. (2005). Movements were also seen in the other three clouds over the shorter periods of time they were visible. The windspeed measured for the major polar cloud was consistent with the more poorly determined windspeeds (1-sigma uncertainty of about 10 m s^{1}) observed for these other features.

2.9. Titan cloud variability

Evidence of substantial temporal variability in the spatial distributions of clouds was observed by VIMS between the second and third pass of Titan in October and December 2004. As shown in Figure 14(b), while clouds persist over the SPR in both views taken seven weeks apart, two prominent cloud features not visible in October appeared in the December image near 41° and 58° S latitude. The two clouds cover a comparable range of latitudes, extending approximately 6.5° or ~290 km. However, unlike the round polar cloud, these features have a streaked appearance, extending significantly further zonally than meridionally. The most equatorward cloud is six times longer in the longitudinal dimension than the latitudinal, while the more southern cloud is 2.5 times longer. This streaked appearance suggests that the windfield is predominantly zonal at temperate latitudes and may exhibit strong vertical and/or latitudinal gradients (shears) in this zonal component.

2.10. Titan emissions

Titan glows in its own emissions both day and night, as strikingly shown in Figure 15. As on Saturn, CH_4 fluoresces on Titan's dayside, as has been observed from the ground (cf. Kim et al., 2000). In this unique VIMS view from a phase angle of 109° – at a vantage point nearly above the terminator – CH_4 fluorescence can be directly mapped for some 730 km above the surface, with a maximum brightness near 350-km altitude. As with Saturn, we are presently analyzing the variation of such fluorescence

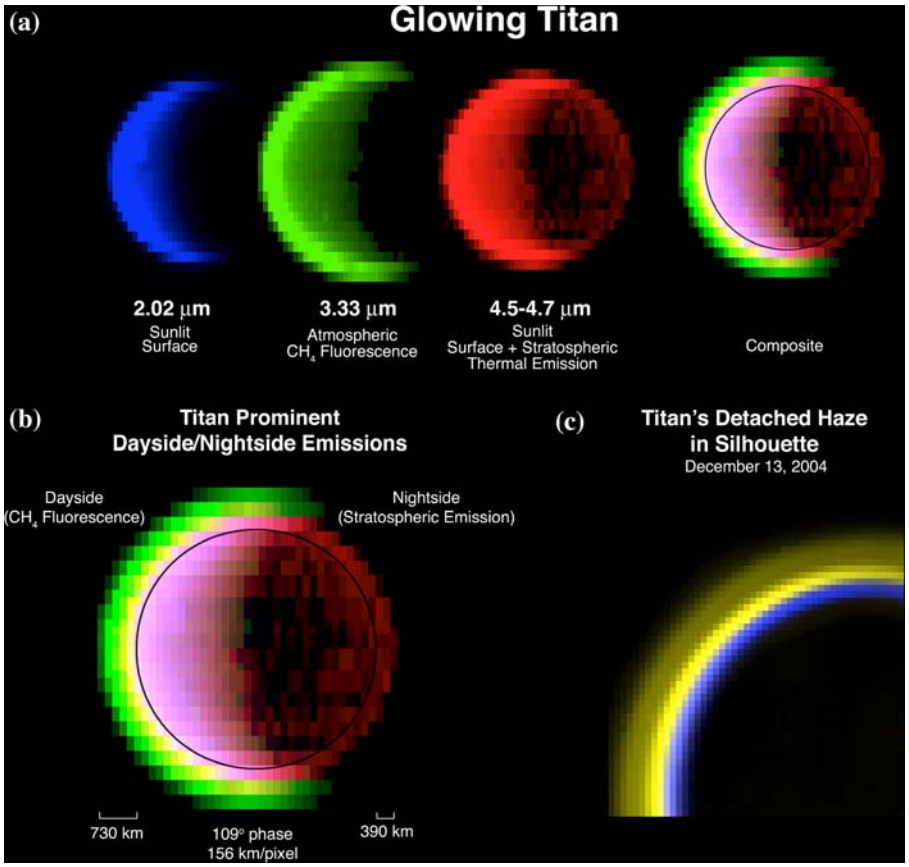

Figure 15. Glowing Titan. Panels (a) and (b) Observation CM1467517212 acquired near 109° phase angle on July 3, 2004 shows emissions on both the dayside and nightside. Here, the dayside emission (green on left side of disk) is due to CH_4 fluorescence near 3.3 μm; the nightside emission (right side of disk, red) is near 4.7 μm, and is likely due primarily to CO emission. Image acquired from 0.621 million km in high-resolution mode, exposure time 400 ms per pixel. Panel (c) High-resolution image of Titan's limb at high phase angle showing CH_4 fluorescence (3.3 μm, yellow) and underlying surface (at 5.1 μm, blue). Dark lane in fluorescent glow is due to aerosol absorption in a haze layer located at about 350 km altitude.

with phase angle, to better determine latitudinal variations in CH_4 abundances at mesospheric levels (~400–600 km altitude) from pole to pole.

As discovered in these first spectral maps of the nightside, Titan glows at night. Emissions shown in red on the rightside of Figure 15 are produced by CO, CO_2, and CH_3D in the 4.2–5.1 m region, as clearly shown in the emission spectrum (Figure 16). Previous dayside observations by Lellouch et al. (2003, 2004) demonstrated the existence CO emissions imbedded within the broader CO absorptions, but their interpretation was complicated by non-LTE effects prevalent on the dayside. Here, these nightside emissions are

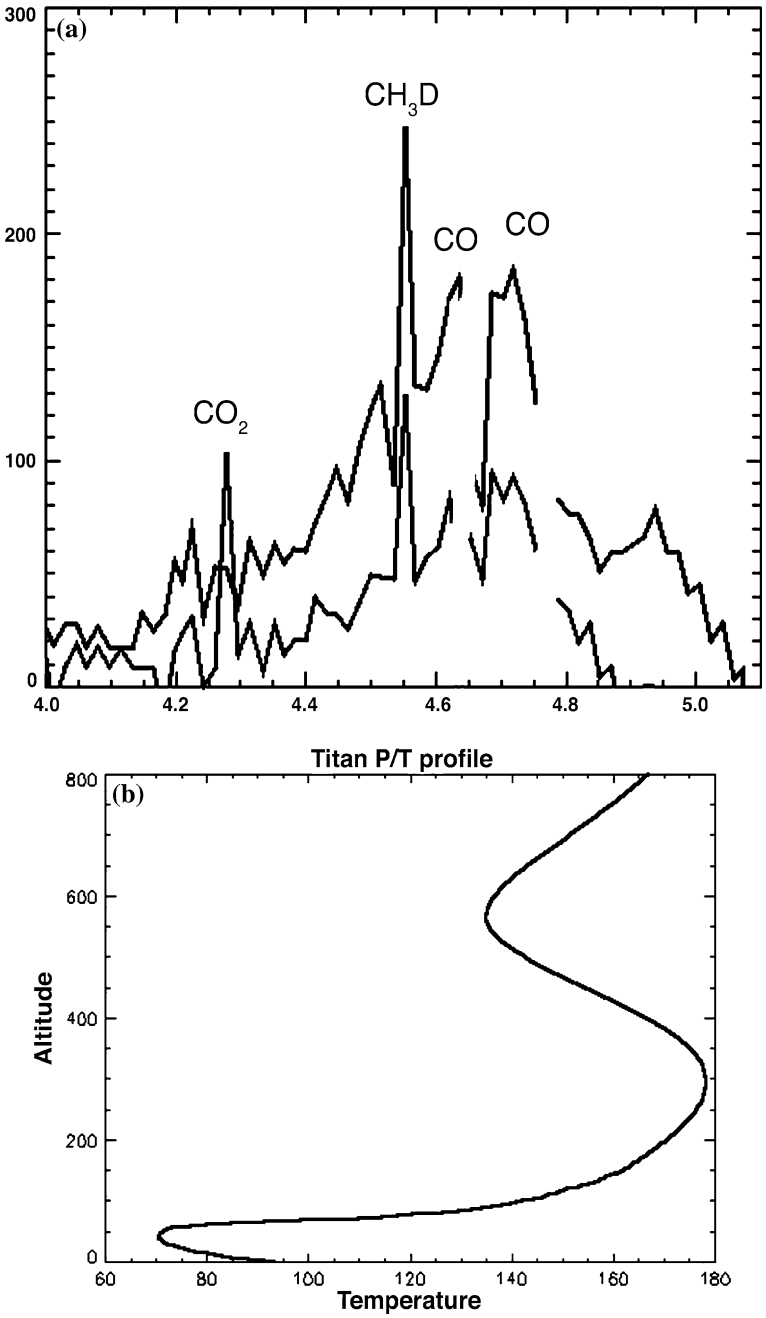

Figure 16. 4.7-μm emission spectra from the limb of Titan. Spectra obtained at approximately 300 km altitude (upper spectrum) and near the surface (lower spectrum). Emissions from CO, CO_2, and CH_3D are observed. Initial modeling indicates a prominent source region near the 300-km-altitude stratospheric temperature maximum (cf. Panel b). Observation CM1467517212 was obtained near 109° phase angle on July 3, 2004 from a distance of 0.621 million km in high-resolution mode and 400 ms per pixel integration time.

primarily thermally induced, emanating largely from the relatively warm stratosphere near the 300 km altitude level. VIMS observations can be used relatively straight-forwardly to constrain the abundances of CO_2, CO, and CH_3D near the 300-km level, and to look for vertical, latitudinal, and temporal variability, perhaps induced by sporadic external delivery of water and other species. These results can also be compared with CIRS results (e.g., Flasar et al., 2005b) to provide information on the vertical distribution of these species. Such work is presently underway.

3. Conclusion

During its first few months in the Saturn system, VIMS atmospheric observations have provided a wealth of exciting new information about the structure, composition, chemistry, and dynamics of Saturn and Titan. Future observations of stellar and solar occultations, increased scrutiny at high spatial resolution over an extensive range of phase angles, and new polar views, all promise to provide important further clues on dynamical and chemical processes taking place within the atmospheres of the outer solar system.

Acknowledgements

We thank Cassini/VIMS team members John Ivens, Dyer Lytle, Dan Moynihan and Bob Watson for much help in the sequence generation and data reduction of the maps and spectra used in this paper. We also thank Linda Brown for helpful discussions regarding phosphine, ammonia, and methane absorption features. A portion of the research described in this paper was carried out at the Jet Propulsion Laboratory, Pasadena, CA, under a contract with the National Aeronautics and Space Administration.

References

Atreya, S. S.: 1986, *Atmospheres and Ionospheres of the Outer Planets and Their Satellites*, Springer, Berlin.

Baines, K. H., Smith, W. H., and Alexander, C.: 1989, in M. J. S. Belton, R. A. West and J. Rahe (eds.), *Time Variable Phenomena of the Jovian System*, NASA Special Publication Vol. 494, pp. 363–370.

Baines, K. H., Brown, R. H. Cruikshank, D. P., Clark, R. N., Nelson, R. M., Matson, S. L., Buratti, B., Carusi, A., Corodini, A., Bibring, J. P., Sotin, C., Jaumann, R., Formisano, V., Combes, M., Drossart, P., Langevin, Y., and Sicardy, B.: 1992, in *Symposium on Titan, Conference Proceedings*, ESA SP-338, pp. 215–219.

Baines, K. H., West, R. A., Giver, L. P., and Moreno, F.: 1993, *J. Geophys. Res. Planets* **98**(E3), 5517–5529.

Borysow, A.: 1992, *Icarus* **96**, 160–175.

Brown, R. A., Baines, K. H., Bellucci, G., Bibring, J.-P., Buratti, B. J., Capacionni, F., Cerroni, P., Clark, R. N., Coradini, A., Cruikshank, D. P., Drossart, P., Formisano, V., Jaumann, R., Langevin, Y., Matson, D. L., McCord, T. B., Mennella, V., Miller, E., Nelson, R. M., Nicholson, P. D., Sicardy, B., and Sotin, C.: 2004, *Space Sci. Rev.* **115**(1-4), 111–168.

Brown, R. A., Baines, K. H., Bellucci, G., Buratti, B. J., Capacionni, F., Cerroni, P., Clark, R. N., Coradini, A., Cruikshank, D. P., Drossart, P., Formisano, V., Jaumann, R., Langevin, Y., Matson, D. L., McCord, T. B., Mennella, V., Nelson, R. M., Nicholson, P. D., Sicardy, B., Sotin, N., Baugh, C., Griffith, C., Hansen, G., Hibbitts, K., and Showalter, M.: 2005, *Astron. Astrophys.* in press.

Butler, R. A. H., Sagui, L., Kleiner, I., and Brown, L. R.: 2005, *J. Mol. Spectrosc.* submitted.

Courtin, R., Gautier, D., Marten, A., Bezard, B., and Hanel, R.: 1984, *Astrophys. J.* **61**, 531–537.

Drossart, P., Th. Fouchet, Th., Crovisier, J., Lellouch, E., Encrenaz, Th., Feuchtgruber, H., and Champion, J.-P.: 1999, in *Proceedings of the Conference "The Universe as seem by ISO"*, ESA SP-427, pp. 169–172.

Fegley, M. B. Jr. and Prinn, R. G.: 1985, *Astrophys. J.* **299**, 1067–1078.

Flasar, F. M., Achterberg, R. K., Conrath, B. J., Pearl, J. C., Bjoraker, G. L., Jennings, D. E., Romani, R. N., Simon-Miller, A. A., Kunde, V. G., Nixon, C. A., Bézard, B., Orton, G. S., Spilker, L. J., Spencer, J. R., Irwin, P. G. J., Teanby, N. A., Owen, T. C., Brasunas, J., Segura, M. E., Carlson, R. C., Mamoutkine, A., Gierasch, P. J., Schinder, P. J., Showalter, M. R., Ferrari, C., Barucci, A., Courtin, R., Coustenis, A., Fouchet, T., Gautier, D., Lellouch, E., Marten, A., Prangé, R., Strobel, D. F., Calcutt, S. B., Read, P. L., Taylor, F. W., Bowles, N., Samuelson, R. E., Abbas, M. M., Raulin, F., Ade, P., Edgington, S., Pilorz, S., Wallis, S., and Wishnow, E. H.: 2005a, *Science* **307**, 1247–1251.

Flasar, F. M., Achterberg, R. K., Conrath, B. J., Gierasch, P. J., Kunde, V. G., Nixon, C.A., Bjoraker, G. L., Jennings, D. E., Romani, R. N., Simon-Miller, A. A., Bézard, B., Coustenis, A., Irwin, P. G. J., Teanby, N. A., Brasunas, J., Pearl, J.C., Segura, M. E., Carlson, R. C., Mamoutkine, A., Schinder, P. J., Barucci, A., Courtin, R., Fouchet, T., Gautier, D., Lellouch, E., Marten, A., Prangé, R., Vinatier, S., Strobel, D. F., Calcutt, S. B., Read, P. L., Taylor, F. W., Bowles, N., Samuelson, R. E. Orton, G.S., Spilker, L., Owen, T. C., Spencer, J. R., Showalter, M. R., Ferrari, C., Abbas, M. M., Raulin, F., Edgington, S., Ade, P., and Wishnow, E. H.: 2005b, *Science* **308**, 975–978.

Goody, R. M., West, R., Chen, L., and Crisp, D.: 1989, *J. Quant. Spectrosc. Radiat. Transf.* **42**, 539–550.

Ingersoll. A. P., Beebe, R. F., Conrath, B. J., and Hunt, C. E.: 1984, in T. Gehrels and M. S. Matthews (eds.), *Saturn*, University of Arizona Press, pp. 195–238.

Kim, S. J., Geballe, T. R., and Noll, K. S.: 2000, *Icarus* **147**, 588–599.

Lacis, A. A and Oinas, V.: 1991, *J. Geophys. Res.* **96**, 9027–9063.

Lellouch, E., Coustenis, A., Sebag, B., Cuby, J.-G., Lopez-Valverde, M., Schmitt, B., Fouchet, T., and Crovisier, J.: 2003, *Icarus* **162**, 125–142.

Lellouch, E., Schmitt, B., Coustenis, A., and Cuby, J.-G.: 2004, *Icarus* **168**, 209–214.

Lewis, J. S. and Fegley, M. B. Jr.: 1984, *Space Sci. Revs.* **39**, 163–192.

Ortiz, J. L., Orton, G. S., Friedson, A. J., Stewart, S. T., Fisher, B. M., and Spencer, J. R.: 1998, *J. Geophys. Res. – Planets* **103**, 23051–23069.

Sanchez-Lavega, A., Lecacheux, J., Colas, F., Rojas, J. F., and Gomez, J. M.: 1999, *Planet. Space. Sci.* **47**, 1277–1283.

Smith, B. A., Soderblom, L., Beebe, R., Boyce, J., Briggs, G., Bunker, G., Collins, S. A., Hansen, C. J., Johnson, T. V., Mitchell, J. L., Terrile, R., Carr, M., Cook, A. F. II., Cuzzi, J., Pollack, J. B., Danielson, G. E., Ingersoll, A. P., Davies, M. E., Hunt, G. E., Masursky, H., Shoemaker, E., Morrison, D., Owen, T., Sagan, C., Veverka, J., Strom, R., and Suomi, V. E.: 1981, *Science* **212**, 163–190.

Smith, B. A., Soderblom, L., Batson, R., Bridges, P., Inge, J., Masursky, H., Shoemaker, E., Beebe, R., Boyce, J., Briggs, G., Bunker, G., Collins, S. A., Hansen, C. J., Johnson, T. V., Mitchell, J. L., Terrile, R., Cook, A. F. II., Cuzzi, J., Pollack, J. B., Danielson, G. E., Ingersoll, A. P., Davies, M. E., Hunt, G. E., Morrison, D., Owen, T., Sagan, C., Veverka, J., Strom, R., and Suomi, V. E.: 1982, *Science* **215**, 504–537.

Sotin, C., Jaumann, R., Buratti, B. J., Brown, R. H., Clark, R. N., Soderblom, L.A., Baines, K. H., Belluci, G., Bibring, J.-P., Capaccioni, F., Cerroni, P., Combes, M., Coradini, A., Cruikshank, D. P., Drossart, P., Formisano, V., Langevin, Y., Matson, D. L., McCord, T. B., Nelson, R. M., Nicholson, P. D., Sicardy, B., LeMouelie, S., Rodriguez, S., Stephan, K., and Scholz, C.K.: 2005, *Nature* **435**, 786–789.

Tomasko, M. G., West, R. A., Orton, G. S., and Tejfel, V.: 1984, in T. Gehrels and M. S. Matthews (eds.), *Saturn*, University of Arizona Press, pp. 150–194.

Toon, O. B., McKay, C. P., Griffith, C. A., and Turco, R. P.: 1992, *Icarus* **95**, 24–53.

Yanamandra-Fisher, P. A., Orton, G. S., and Fisher, B. M.: 2001, *Icarus* **150**, 189–193.